FRONTIERS OF PHYSICS

RESEARCH ARTICLE
Volume 21 / Issue 5 / 054201 / 2026

A device harnessing capacitive-coupled memristive effects for leaky integrate-and-fire neuron and electrocardiogram signal recognition implementation

Jingjuan Wang[1], Biao Yang[2], Hui He[2], Changliang Li[2], Xiaobing Yan[2,†]

1 Intelligent Sensor Network Engineering Research Center of Hebei Province, Hebei Key Laboratory of Optoelectronic Information and Geo-detection Technology, College of Information Engineering, Hebei GEO University, Shijiazhuang 050031, China
2 Key Laboratory of Brain-Like Neuromorphic Devices and Systems of Hebei Province, College of Electron and Information Engineering, Hebei University, Baoding 071002, China
Corresponding author. E-mail: †xiaobing_yan@126.com
Received August 25, 2025; accepted September 29, 2025

© Higher Education Press 2026

ABSTRACT

Artificial neurons are essential for constructing neuromorphic networks, enabling information computation with high parallelism and efficiency akin to the human brain. Nonetheless, artificial synapses fabricated from conventional silicon-based materials exhibit limited adaptability in complex biological environments, making it challenging for them to replicate the intricate synaptic plasticity of biological synapses. In this work, Pt/$La_{0.5}Sr_{0.5}CoO_3$(LSCO)/BST:CeO_2/LSCO parallel-plate capacitor structure devices with capacitive-coupled memristive effects were fabricated. The current–voltage curves of the device under different voltages were investigated, revealing a remarkable evolution of the device from capacitive-dominated responses to pure memory behaviors. The pure memristive state of the device was utilized to simulate biological synaptic functions, while the capacitive-coupled memristive effects serve as the linchpin for emulating biological neuronal functionalities. By integrating these devices into bespoke circuits, leaky integrate-and-fire (LIF) functions are faithfully replicated, encompassing the precise mimicry of leakage, spatiotemporal integration, and firing processes. Moreover, a spiking neural network (SNN) based on the devices was constructed to identify the electrocardiogram (ECG) data sets to realize the diagnosis of diseases with a recognition accuracy of 91%. The research findings thus herald a significant stride in neuromorphic computing, proffering a potent avenue for architecting brain-inspired computational frameworks.

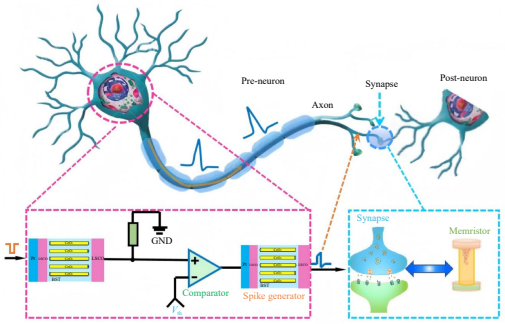

Keywords capacitive-coupled, $Ba_{0.6}Sr_{0.4}TiO_3$, leaky integrate-and-fire, electrocardiogram signal

1 Introduction

Artificial neurons are crucial for constructing neuromorphic systems. Although CMOS-based circuits have been the most common approach for implementing artificial neurons [1–3], they suffer from limitations such as low

https://doi.org/10.15302/frontphys.2026.054201

integration density and high power consumption. The development of alternative scalable neurons, including those based on memristors, is therefore essential for building large-scale neuromorphic computing systems. Biological neurons transmit and process information by spatiotemporally integrating input signals and firing action potentials [4, 5]. Several models have been developed to mimic these behaviors, including the McCulloch-Pitts (MP) [6], Hodgkin-Huxley (H-H) [7], Integrate-and-Fire (IF) [8], and Leaky Integrate-and-Fire (LIF) models [9]. The IF model, pioneered by Louis Lapicque in 1907, offers a simplified mathematical framework for neuronal dynamics [10]. It describes how a neuron integrates synaptic inputs until its membrane potential reaches a threshold, triggering a spike followed by reset [11]. While computationally efficient, the IF model lacks biological realism by omitting membrane potential leakage. The LIF model addresses this by incorporating a leakage term that mimics the natural decay of membrane potential, providing a more physiologically plausible representation [12]. The LIF model is particularly valuable for spiking neural networks due to its ability to simulate leakage, spatiotemporal integration, and firing functions inherent to biological neurons. In biological systems, these short-term dynamics arise from ion concentration differences across the cell membrane, which generate capacitive-like effects. Interestingly, similar capacitive effects occur in many memristive devices [13], enabling the implementation of LIF behaviors with suitably designed circuits. Thus, memory devices exhibiting capacitive effects are promising for constructing neurons with leaky integration and firing capabilities.

Both memristors and capacitors possess similar two-terminal structures, with a dielectric layer sandwiched between two metal electrodes. Therefore, memristors can exhibit capacitive characteristics during the operating stage under certain conditions. Up to now, the influence of the capacitive-coupling memory effect has been observed in many memristors [14–16]. In addition, it has been found that numerous ferroelectric materials, such as $Ba_{0.6}Sr_{0.4}TiO_3$ (BST) [17], $BaTiO_3$ (BTO) [18], $Pb(Zr_{0.4}Ti_{0.6})O_3$ (PZT) [19] and so on, can be used not only as parallel-plate capacitors but also as the dielectric layers of memristors. However, due to the high dielectric constant of ferroelectric materials, their tunability is limited. Introducing another substance to form a composite structure with ferroelectrics is a promising method for developing new materials with special coupling properties suitable for exploitation. Among the above materials, the $Ba_{0.6}Sr_{0.4}TiO_3$ (BST) compound has been widely used in tunable microwave devices and dynamic memory devices due to its material properties of high dielectric constant and low dielectric loss [17]. Additionally, CeO_2 has been widely applied in memristor devices because of its high oxygen ion conductivity, valence states of copper ions, inherent resistive switching (RS) characteristics, large on/off ratio, remarkable plasticity and compatibility with current CMOS technology [20–22]. Recent studies have further highlighted the potential of advanced materials in optimizing memristor performance, providing valuable references for the design of composite structures [23–25]. In oxide-based memristors, the capacitive effect is mainly attributed to the migration of oxygen ions. Hence, the composite thin-film devices combining BST and CeO_2 are expected to achieve the characteristics of capacitive-coupling memory.

Notably, existing studies have explored memristor-based implementations of neuromorphic systems with functionalities relevant to LIF neurons, such as the brain-inspired in-memory computing system leveraging memristive circuits for neuronal communication [26], the multimodal local-global neuromorphic computing system (MLG-NCS) for affective video content analysis [27], and the time-frequency hybrid neuromorphic architecture for battery state-of-health estimation [28]. Unlike these works that focus on system-level integration for specific tasks (neuronal communication, affective analysis, battery estimation), this study specifically emphasizes optimizing memristive device-level capacitive effects to enhance the biological realism and scalability of LIF neuron implementations, addressing the trade-off between computational efficiency and physiological plausibility that is less highlighted in the aforementioned task-oriented systems.

Herein, this study proposes and fabricates a $Pt/La_{0.5}Sr_{0.5}CoO_3$(LSCO)/BST:CeO_2/LSCO device with capacitive-coupled memristive effects. High-quality BST:CeO_2 composite films were deposited on single-crystalline $SrTiO_3$ (STO) substrates through a series of techniques such as magnetron sputtering and pulsed laser deposition. Initially, the structural and elemental characteristics of the device were thoroughly investigated. Under electrical modulation, the device's transition from capacitive behavior to pure memory behavior was revealed by varying the voltage magnitude. Furthermore, the device's capacity to mimic a variety of biological synaptic functions in the pure memristor state was explored. Through integrating the device into a custom-designed circuit, the LIF function was simulated. Especially, based on spiking neural network (SNN), this device is expected to be applied to monitor heartbeats and could early diagnose cardiovascular diseases. Thereby, this research lays a solid foundation for the development of advanced neuromorphic computing systems with augmented performance and functionality.

2 Result and discussion

Figure 1(a) presents the structure of the Pt/LSCO/BST:CeO_2/LSCO device. The cross-sectional TEM

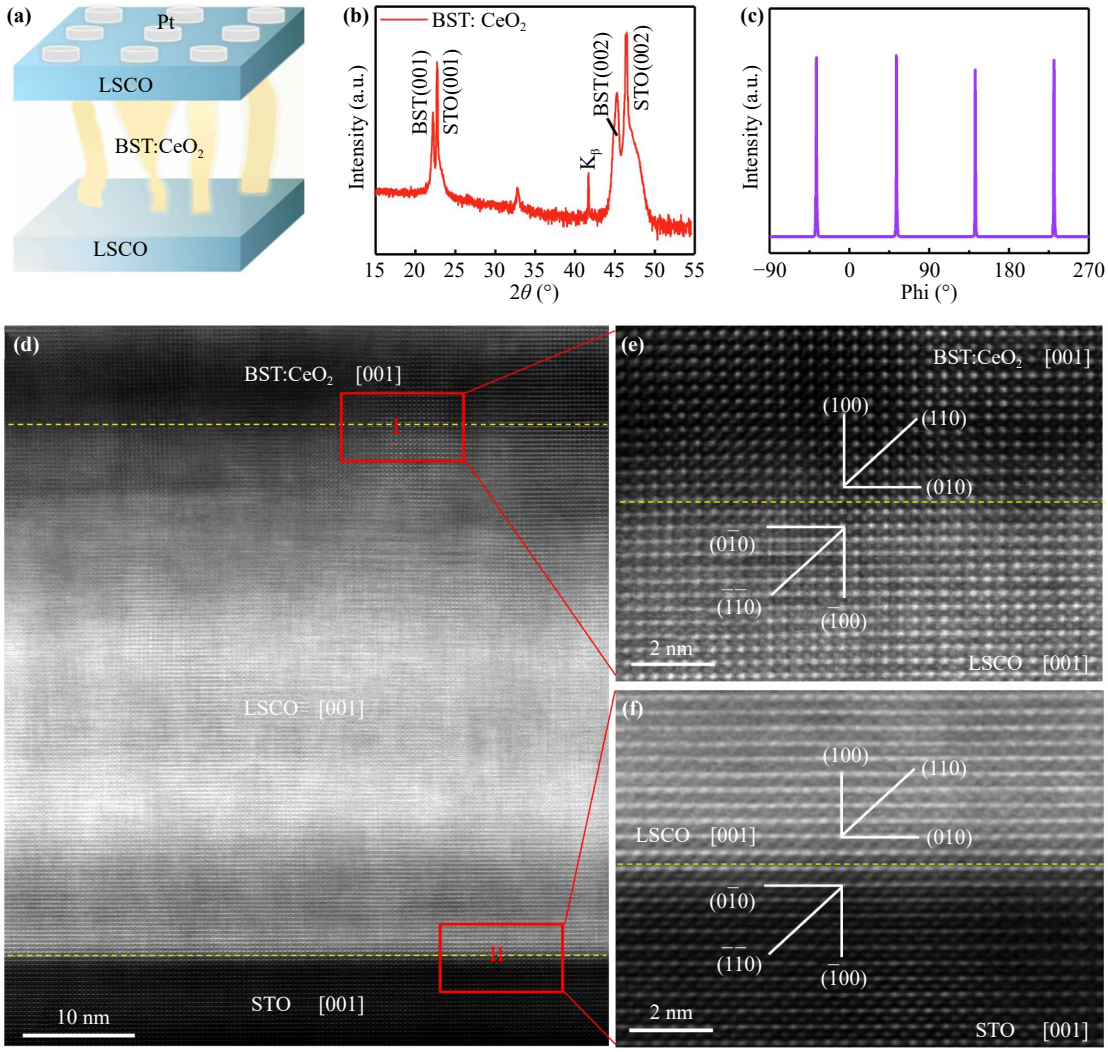

Fig. 1 **(a)** Schematic illustration of the Pt/LSCO/BST:CeO_2/LSCO device. **(b)** The XRD θ–2θ scanning results. **(c)** Φ-scanning profiles of the BST:CeO_2 film. **(d–f)** HRTEM analysis of Pt/LSCO/BST:CeO_2/LSCO device. (d) The interfacial relationship between the LSCO layer and the adjacent BST:CeO_2 layer as well as the STO layer respectively. (e) The magnified image of the red region (I) within (d) is presented, wherein the BST:CeO_2/LSCO interface exhibits an almost perfectly coherent growth pattern. (f) The magnified image of the red region (II) in (d), which represents the LSCO/STO(001) interface.

image of the device is shown in Fig. S1. Meanwhile, the EDS elemental mapping results have effectively verified the elemental distribution within the Pt/LSCO/BST:CeO_2/LSCO device, as depicted in Fig. S2. Figure S2(b) shows the element distribution of Pt (top electrode). In Figs. S2(c)–(i), the elements La, Ti, Co, Ce, Sr, O, and Ba were uniformly distributed in the dielectric layer, indicating that the chemical composition of the Pt/LSCO/BST:CeO_2/LSCO was homogeneous. The X-ray diffraction (XRD) spectra (Fig. 1(b)) shows the BST thin films display a (001) orientation with respect to the STO substrate, indicating the successful formation of pure perovskite thin films. The Φ-scanning of the BST (001) planes, in view of the tetragonal BST crystal structure, the four peaks are uniformly distributed, which reveals the fourfold symmetry of the epitaxial BST film, as shown in Fig. 1(c). To further prove this conclusion, the highresolution transmission electron microscopy (HRTEM) images of the initial Pt/LSCO/BST:CeO_2/LSCO device are shown in Figs. 1(d)–(f), in which clear lattice fringes can be observed. The crystal plane indices, such as (001), (100), and (110), indicate a consistent crystal orientation relationship among the BST:CeO_2, LSCO, and STO layers at the interfaces. As revealed in Fig. 1(e), the atom positions near the interface can be clearly resolved, indicating that the BST:CeO_2 film grew perfectly and coherently on the LSCO (bottom electrode) lattice because they have the same type of crystal structure and almost same lattice constants. Moreover, the interfaces between the material

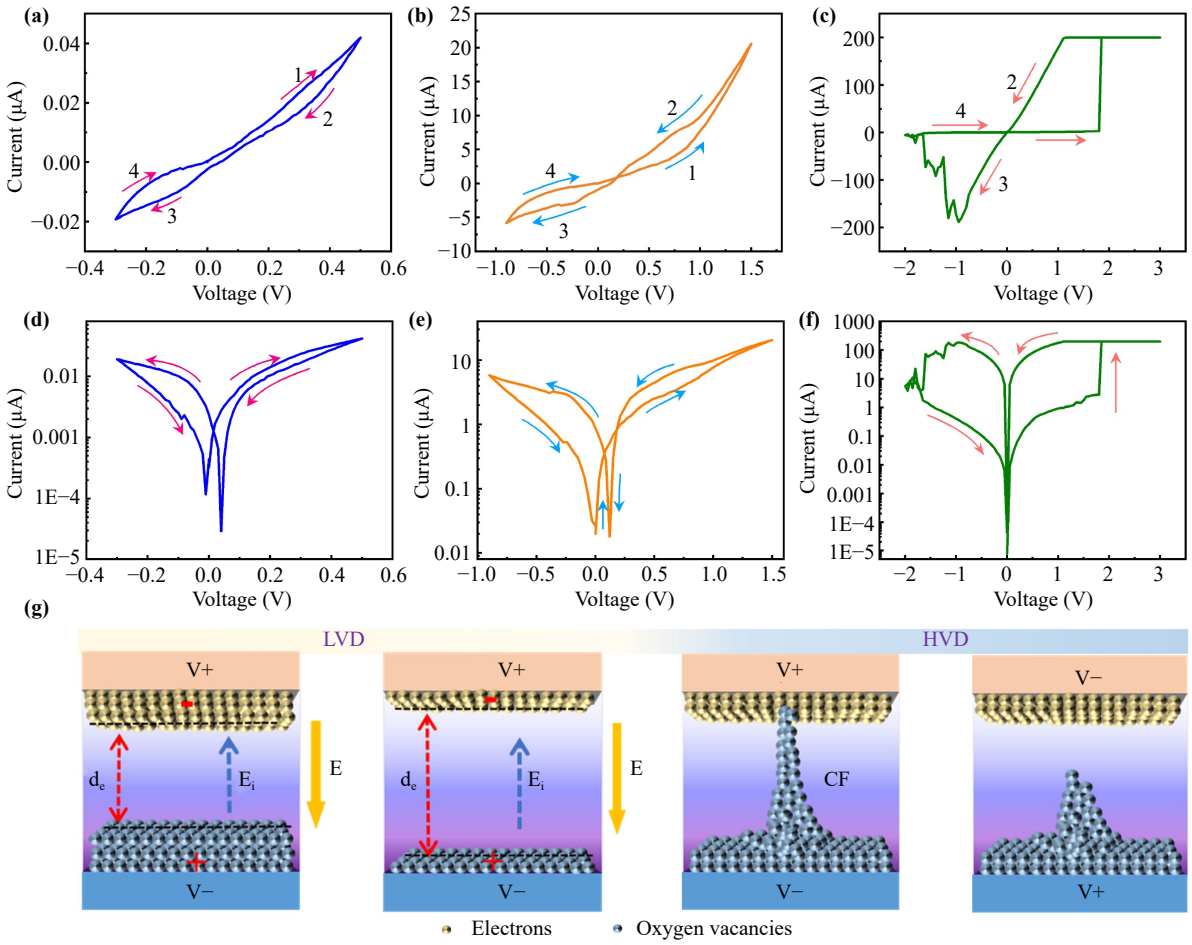

Fig. 2 **(a–c)** *I–V* curves under different voltage windows. **(d–f)** Corresponding logarithmic *I–V* curves. **(g)** Schematics showing the electrons and oxygen vacancy diffusion processes.

layers are highly flat without any noticeable lattice distortion or defects. The flatness of the interfaces is beneficial for reducing interface scattering, thereby enhancing the electrical performance of the device. Additionally, the lattice fringes in the images are extremely sharp, suggesting that the crystal structures of the materials are nearly perfect with minimal crystal defects. These observations collectively confirm the superior epitaxial properties of the device, indicating its potential for excellent performance in high-performance electronic device applications.

Subsequently, in order to investigate the electrical properties of the device, *I–V* measurements were carried out on the Pt/LSCO/BST:CeO_2/LSCO device. A voltage was applied to the tested devices and scans were executed between V_{max} (maximum applied voltage) at a constant scanning rate of 0.01 V/s. The acquired *I–V* curves with V_{max} values of 0.5, 1.5, and 3.0 V are illustrated in Figs. 2(a)–(c) (linear scale) and Figs. 2(d)–(f) (logarithmic scale), respectively. At V_{max} of 0.5 V, Figs. 2(a) and 2(d) show that the *I–V* curve has a non-zero crossing without an intersection point. It is well known that such a non-zero-crossing *I–V* curve indicates the existence of a capacitive effect in the memristor [29–33]. Upon increasing V_{max} to 1.5 V, a crossing behavior manifested within the *I–V* curve was discernible [Fig. 2(b)], with the intersection point situated in the first quadrant [Fig. 2(e)]. Nevertheless, this *I–V* curve remained non-zero-crossing. When the test voltage was further increased to $V_{max} = 3.0$ V, a zero-crossing *I–V* hysteresis curve indicating the standard memory behavior of the device was observed [Figs. 2(c) and (f)]. These *I–V* characteristics are reproducible and can be controlled by selecting V_{max}. The above investigations reveal that by augmenting V_{max}, the transformation of the device from capacitive behavior to capacitively-coupled memory behavior and ultimately to pure memory behavior can be accomplished. Based on the above analysis, further research on the pure memristive performance of the device was conducted. The device exhibits stable memristive behavior with over 100 cycles of operation without significant degradation, and the high and low

resistance states are well-defined and concentrated, as shown in Fig. S3. Furthermore, its intrinsic memristive properties enable the emulation of biological synapse functions (Fig. S4). Figure 2(g) illustrates the carrier transport mechanism in the functional layer of the device, showing the transitions between the HRS and the LRS in both the low voltage district (LVD) and the high voltage district (HVD) of the device. It can be seen that when a positive voltage is applied to the Pt electrode of the device, the positively charged oxygen vacancies (V_o^{2+}) in the BST:CeO_2 functional layer will move towards the bottom electrode along the direction of the electric field, and shield the negatively charged region at the bottom interface. The positive and negative ions (V_o^{2+} and O^{2-}) moving in the electric field carry displacement current, resulting in a capacitive effect in the functional layer at low voltages. The displacement current presents a non-zero-crossing I–V curve [34]. Moreover, as the voltage increases, the ion concentration increases correspondingly, which further alters the memory behavior caused by the internal electromotive force [35], so the capacitive-coupled memory effect will be exhibited in the device. Under the application of a high voltage, local Joule heating is generated in the device due to the high current, improving the mobility of oxygen vacancies, and the high electric field can effectively accelerate the migration of electrons and ions [36–40]. After reaching a certain threshold, conductive filaments (oxygen vacancies) will eventually form within the BST:CeO_2 composite oxide layer. Once the conductive filaments are formed, they provide a path for the conductive current to move between the two electrodes, surpassing any displacement current. At this time, the capacitive effect is largely suppressed completely, and a pure memory effect is exhibited. After the voltage polarity is reversed, due to the Coulomb repulsion effect, the oxygen vacancies are pushed back to the top electrode, causing the conductive filaments to partially dissolve and form a relatively large gap in the functional layer. The carriers of the conduction current are expected to pass through this gap [41, 42]. Therefore, after such a reset process, the device returns to the HRS, and this process under high voltage is similar to that reported in standard memristive devices.

Based on the capacitive-coupled memristive characteristic of the device, it can be incorporated into a circuit to demonstrate an artificial neuron with leaky, integrate and fire functions. The physical diagram is shown in Fig. S5. In biological neurons, the difference of ion concentration inside and outside cells leads to leaky integrate-and-fire potential (LGP) with short-term kinetics. The difference of ion concentration can induce the cell with concentration change. This effect has been widely used in many memristor devices [30]. Ion migration in the switching process of memristor will produce an internal electric field, which can realize short-term dynamic changes and can be used to simulate LGP in biological neurons. More interestingly, the capacitive effect can simulate the hyper potential of biological spikes. As shown in Fig. 3(a), a simple circuit can be designed by using the capacitive-coupled memristive devices to realize LIF function, so as to simulate the process of neuronal transmission.

Therefore, the memristive device with capacitive effect is very important to construct neurons with LIF function. The circuit of the artificial neuron with LIF functions is shown in Fig. 3(b). The circuit contains two devices M1 and M2 of Pt/LSCO/BST:CeO_2/LSCO structure. An input signal is applied on M1 to simulate LGP. When the LGP exceeds the threshold, the comparator generates a rising edge and emits a pulse to stimulate M2. The voltage on R_3 (1 kΩ) is emitted as a spike similar to biological excitation. In a biological neuronal system, each neuron transmits neural signals through multiple synapses. When a number of dendrites of a neuron receive signals simultaneously, these signals will be summed together in a process called spatial integration. Temporal integration is the sum of the signals arriving at different frequencies of the neuron. Therefore, by controlling the amplitude and frequency of the input pulses applied to M1, the conductance of M1 can be changed to simulate the spatial and temporal integration of the LGP. A spike output will be generated when LGP is above the threshold, and the conductance of M1 will slowly recover to the high resistance state when the input stimulus is small.

To investigate the response of the neuron device to input signals, we first applied input pulses with a fixed pulse width of 0.1 ms and a fixed pulse interval of 0.5 ms, while adjusting the pulse amplitudes to four specific values: –0.5 V, –0.8 V, –1 V, –1.3 V, –1.5 V, and –1.8 V, as illustrated in Fig. 4(a). When the sum of these input signals (with the aforementioned pulse parameters) arriving simultaneously at the neuron reaches a sufficiently high level, the LGP will rise above the preset threshold (250 mV, consistent with the threshold setting in the LIF circuit described earlier), at which point a spike output will be generated. Figure 4(b) simulates temporal integration by varying the frequency of the input pulse signal, with the input pulse amplitude fixed at –1.5 V and frequencies set to 1 kHz, 1.25 kHz, 1.67 kHz, 2.5 kHz, and 5 kHz respectively. When the frequency of the input signal is low (1 kHz) the neuron will not produce output spikes. When the frequency of the input signal is high enough, output spikes will be generated and the frequency of the spike output will increase as the frequency of the input signal increases. To further verify the firing conditions of the device, six continuous voltage pulses with different frequency ranges (from 1 kHz to 3 kHz) and different amplitude ranges (from –0.5 V to –2 V) were applied to the neuronal device in various combinations, and the discharge conditions were

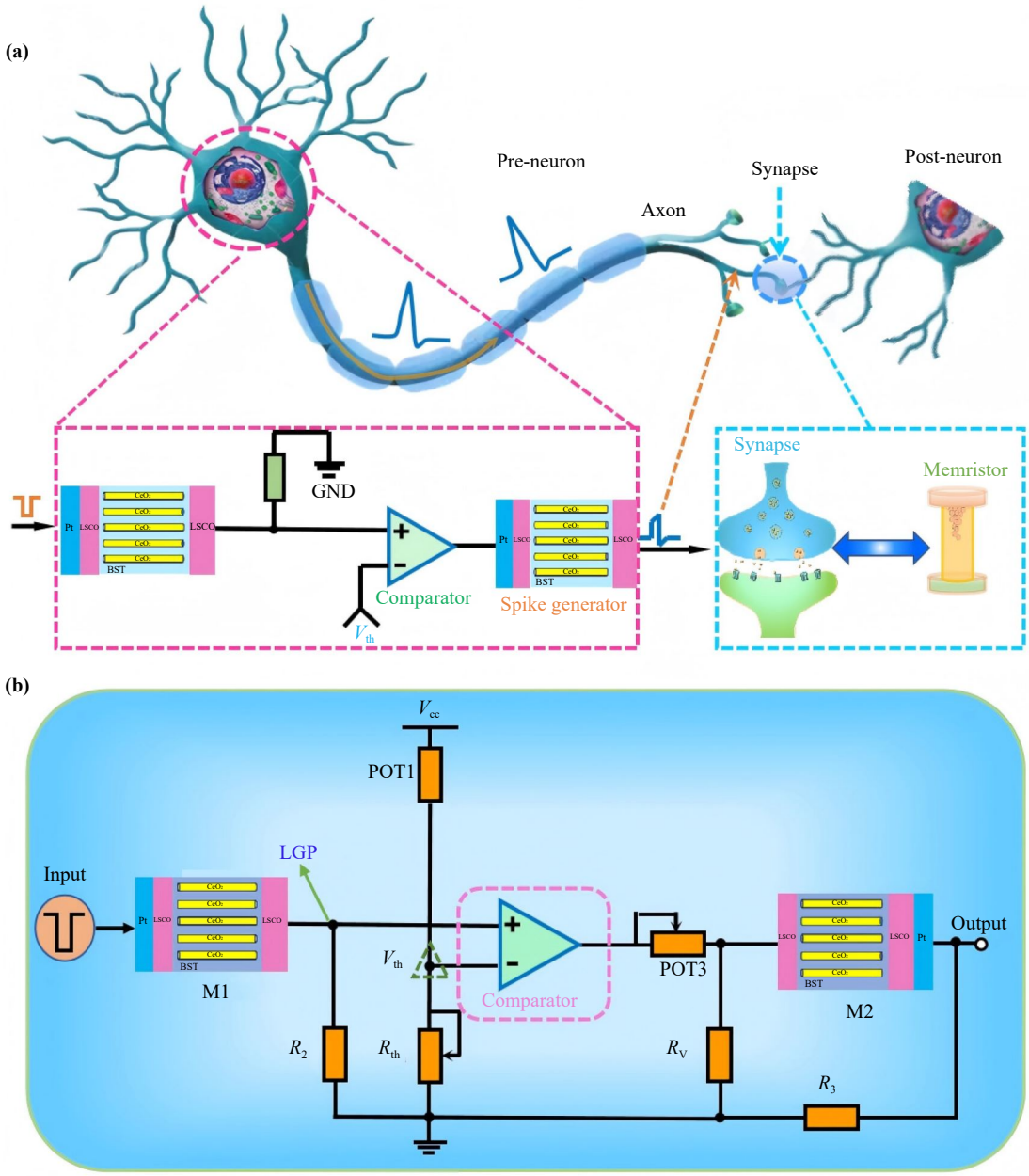

Fig. 3 **(a)** Schematic diagram of biological LIF neuron transmission and corresponding circuit simulating neuron transmission function. **(b)** The function of LIF neurons is realized through the device with the structure of Pt/LSCO/BST:CeO_2/LSCO and the designed pure circuit.

recorded [Figs. 4(b)–(e)]. As depicted in Fig. 4(d), according to the differences in the applied conditions, it can be divided into two regions: the non-firing region (pink) and the firing region (green). When the frequency and amplitude are relatively small, the generated LIF potential (LGP) cannot reach V_{th} [Fig. 4(c)], which corresponds to the non-firing condition. As the frequency and amplitude increase, the LIF neuron gradually transitions to the firing region and finally reaches the firing state [Fig. 4(e)]. The statistical results are instructive for the selection of experimental parameters in subsequent work.

Based on the properties of the LIF neuron circuit validated by the above tests, a SNN for arrhythmia classification was constructed to verify the effectiveness of this LIF neuron circuit in biomedical signal processing tasks. The network structure is shown in Fig. 5(a), employing a two-layer fully connected architecture. The input layer node count matches the feature dimension of the ECG signals, set to 235, corresponding to the number of features in a single ECG signal from the MIT-BIH arrhythmia database. The output layer contains four

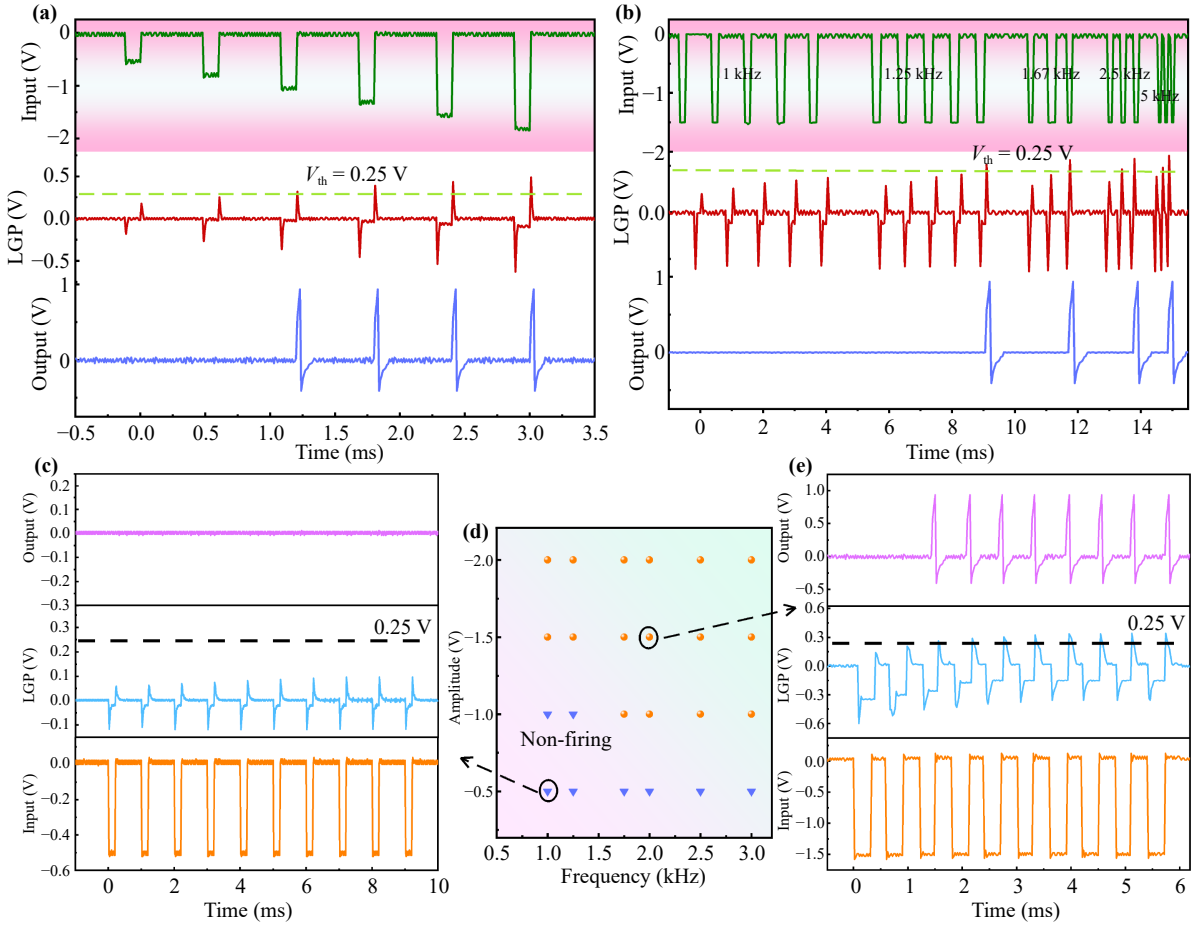

Fig. 4 **(a)** Spatial integration and bioinspired fire realized with the circuit. **(b)** Temporal integration and bioinspired fire realized with the circuit. **(c)** Statistical diagram of fire state of neuron model (input signal frequency and amplitude). Input 10 continuous voltage pulses to count the fire conditions. The lower left (pink area) is in non-fire state, and the upper right (green area) is in firing state schematic diagram of **(d)** non-firing state **(e)** firing state.

neurons, each corresponding to one of the four rhythm categories. In the data processing stage, a rate-coding strategy was used to convert continuous ECG signals into spike trains. Specifically, each sample was divided into 10 time steps along the temporal dimension, and a binarized spike sequence was generated by comparing randomly generated thresholds with the signal amplitude. This encoding method effectively preserves the signal's amplitude characteristics and provides SNNs with impulse signals compatible with the input characteristics of biological neurons. The experimental data were collected from the MIT-BIH arrhythmia database, which covers diverse arrhythmia types, such as normal sinus rhythm, premature ventricular beats, and premature atrial beats. Four specific categories were selected for training and classification: Normal beat (N), Supra ventricular escape beat (SVEB), Ventricular escape beat (E), and Fusion of ventricular and normal beat (F). After training, the SNN achieved 91% classification accuracy on the test set. The test accuracy over 50 training epochs is shown in Fig. 5(b). The confusion matrix, visualizing the model's classification performance for different arrhythmia categories [Fig. 5(c)], demonstrates effective discrimination across all four ECG data classes. Figure 5(d) displays typical ECG signal samples from each category, along with the outputs of their corresponding output neurons.

These results indicate that the network possesses strong discriminative ability for major arrhythmia types, extracting key features in ECG signals through its spiking patterns. This outcome validates the effectiveness of the LIF neuronal circuit based on BST:CeO_2 memristors in real-world biomedical signal processing tasks, providing a theoretical and experimental foundation for applying memristor-based neuromorphic computing systems in medical diagnosis.

3 Experimental

The device with a structure of Pt/LSCO/BST:CeO_2/LSCO was fabricated on a single-crystalline STO

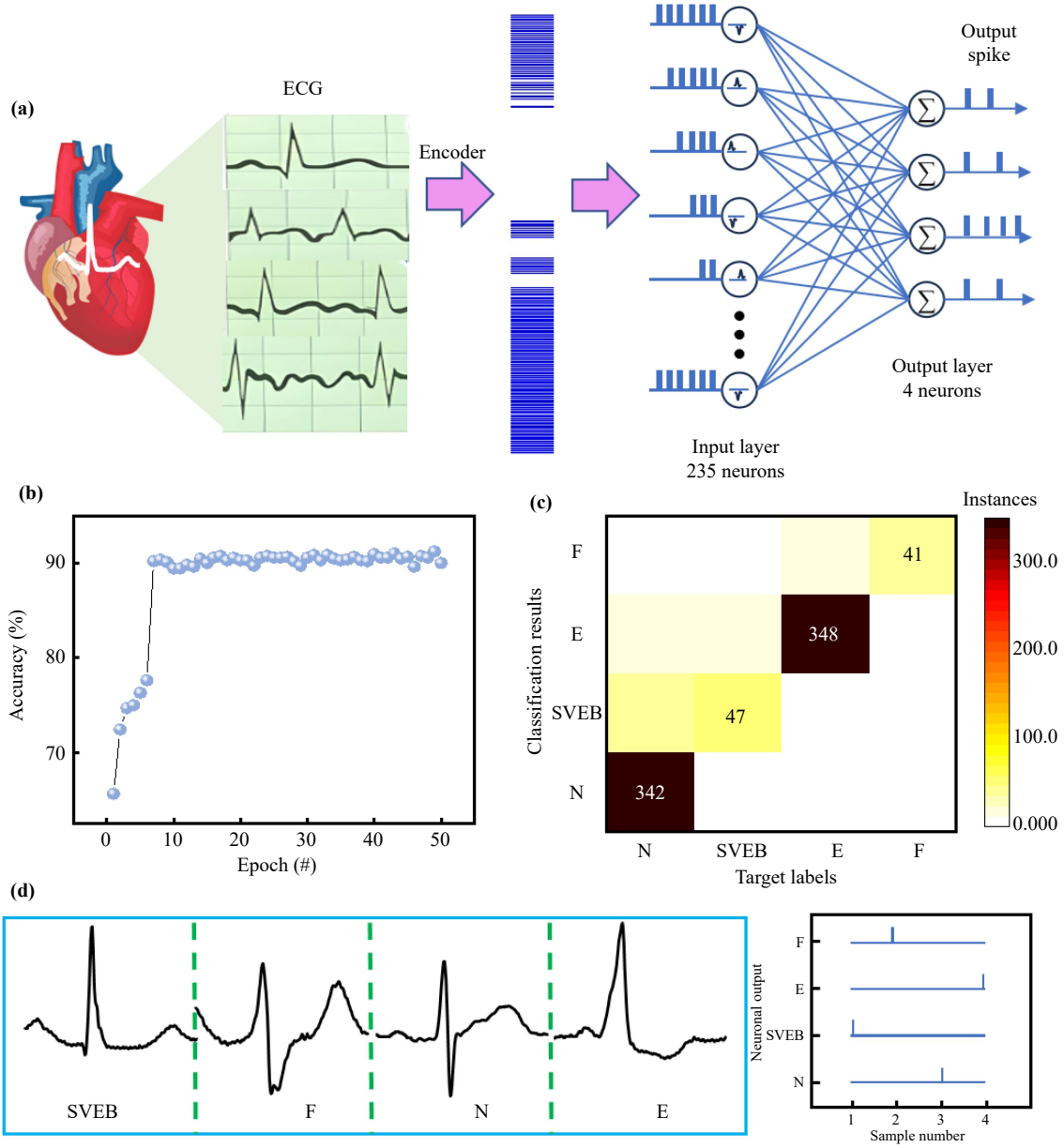

Fig. 5 SNN based on BST:CeO_2 memristor neurons. **(a)** Schematic of SNN network structure. **(b)** Accuracy of SNN after 50 epochs. **(c)** Confusion matrix of recognition results. **(d)** ECG samples of four different classes and the outputs of the corresponding output neurons.

substrate. The specific steps are as follows: the single-crystalline STO was ultrasonically cleaned in acetone and alcohol for 10 minutes respectively to remove surface impurities, and then the cleaned substrate was placed into a magnetron sputtering chamber. Firstly, the chamber was evacuated until reaching a vacuum of 2×10^{-4} Pa, and then the total gas flow rate was configured to 100 sccm with the gas flow ratio of argon to oxygen set at 3:1. After that, the gate valve was precisely adjusted to maintain the pressure at 1.4 Pa, the radio frequency power was set to 50 W and the deposition temperature was set to 550 °C. After pre-sputtering for 20 minutes, formal sputtering was carried out for 30 minutes. The annealing temperature was 600 °C, and the thickness of the grown LSCO thin film was 50 nm. The BST thin film was fabricated via pulsed laser deposition. Initially, the chamber was evacuated to attain a background vacuum of 2×10^{-4} Pa. Subsequently, the gas flow ratio of argon to oxygen was adjusted to 75:25. Concurrently, the deposition pressure within the chamber was stabilized at 5 Pa and the deposition temperature was set at 885 °C. The laser energy was maintained within the range of 314 to 316 mJ, while simultaneously the laser frequency was fixed at 1 Hz. Meanwhile, set

the frequency of magnetron sputtering at 50 W for doping CeO_2. The LSCO thin film with a thickness of 20 nm was repeatedly grown on the BST thin film. Finally, the Pt circular top electrode with the thickness of 50 nm (diameter : 100 μm) was fabricated by means of magnetron sputtering with a mask.

The cross-sectional image was characterized by HRTEM. The crystal structure of BST was characterized by XRD. The DC electrical performance of the device is tested by Keithley 4200SCS source measurement unit. Pulse measurements for the Pt/LSCO/BST:CeO_2/LSCO devices were performed with the Rigol DG5072 function/arbitrary waveform generator and the Rigol DS4022 oscilloscope.

4 Conclusions

Artificial neurons with functions like LIF, and spike output are of utmost importance for highly efficient brain-inspired computing. In this study, a functional layer was formed by integrating $Ba_{0.6}Sr_{0.4}TiO_3$ and CeO_2 within the memory device, which verified its capacitive effect and non-volatile storage capacity. When the voltage was ramped up from zero, the device initially entered a capacitively-coupled memory state at low voltages and subsequently transitioned to a pure memory state at higher voltages. This work not only simulated the biological synaptic plasticity function of the device in the pure memristor state, but also constructed a neuron model that concisely and effectively replicated the LIF functions of biological neurons based on the unique capacitive coupling memristive behavior of the device, thereby demonstrating the reliability of the simulation of neuron transmission. Finally, a SNN based on this device was constructed to recognize the ECG dataset, achieving an identification accuracy of 91%. The above research collectively demonstrated the potential of this capacitive coupling memristive device in neural network applications. Future efforts will focus on enhancing the device's operational stability across varying temperatures and further elucidating the underlying ion migration and capacitive-coupled switching mechanisms. At the circuit level, developing more bio-plausible and energy-efficient neuron models is essential for enabling large-scale, low-power spiking neural networks. On the system level, advanced learning algorithms and robustness to low SNR signals will be prioritized to facilitate real-world biomedical applications, such as real-time health monitoring and edge-computing diagnostics.

Declarations The authors declare that they have no competing interests and there are no conflicts.

Data availability The data that support the findings of this study are available within the article.

Electronic supplementary materials The online version contains supplementary material available at https://doi.org/10.15302/frontphys.2026.054201.

Acknowledgements This research was financially supported by the Youth Fund Project of Hebei Provincial Department of Education (No. QN2024247), the National Preresearch Project of Hebei GEO University (No. KY2024QN17), the Doctoral Initiation Fund of Hebei GEO University (No. BQ2024066), the National Key R&D Plan "Nano Frontier" Key Special Project (No. 2021YFA1200502), and the Cultivation Projects of National Major R&D Project (No. 92164109).

References

1. F. M. Bayat, M. Prezioso, B. Chakrabarti, H. Nili, I. Kataeva, and D. Strukov, Implementation of multilayer perceptron network with highly uniform passive memristive crossbar circuits, *Nat. Commun.* 9(1), 2331 (2018)
2. M. E. Beck, A. Shylendra, V. K. Sangwan, S. Guo, W. A. Gaviria Rojas, H. Yoo, H. Bergeron, K. Su, A. R. Trivedi, and M. C. Hersam, Spiking neurons from tunable Gaussian heterojunction transistors, *Nat. Commun.* 11(1), 1565 (2020)
3. S. Wang, J. Wei, L. Du, C. Wang, and G. Zhao, Challenges and opportunities for memristors in modern AI computing paradigms, *Front. Phys. (Beijing)* 21(3), 035401 (2026)
4. J. Yang, Z. X. Jian, Z. R. Wang, J. H. Zhao, Z. Y. Zhou, Y. Sun, M. Hao, L. Wang, P. Liu, J. Wang, Y. Pei, Z. Zhao, W. Wang, and X. B. Yan, HfAlO-based ferroelectric memristors for artificial synaptic plasticity, *Front. Phys. (Beijing)* 18(6), 63603 (2023)
5. H. Chen, X. G. Tang, Z. Shen, W. T. Guo, Q. J. Sun, Z. Tang, and Y. P. Jiang, Emerging memristors and applications in reservoir computing, *Front. Phys. (Beijing)* 19(1), 13401 (2024)
6. S. Aunet, B. Oelmann, P. A. Norseng, and Y. Berg, Real-time reconfigurable subthreshold CMOS perceptron, *IEEE Trans. Neural Netw.* 19(4), 645 (2008)
7. W. Yi, K. K. Tsang, S. K. Lam, X. Bai, J. A. Crowell, and E. A. Flores, Biological plausibility and stochasticity in scalable VO_2 active memristor neurons, *Nat. Commun.* 9, 4661 (2020)
8. T. Tuma, A. Pantazi, M. Le Gallo, A. Sebastian, and E. Eleftheriou, Stochastic phase-change neurons, *Nat. Nanotechnol.* 11(8), 693 (2016)
9. F. T. Zohora, S. Debnath, and A. H. U. Rashid, Memristor-CMOS hybrid implementation of leaky integrate and fire neuron model, in: 2019 International Conference on Electrical, Computer and Communication Engineering (ECCE), IEEE, 2009
10. L. Lapique, Researches quantatives sur l'excitation electrique des nerfs traitee comme une polarization, *J. Physiol. Pathol. Gen.* 9, 620 (1907)
11. J. Bian, Y. Tao, Z. Wang, X. Zhang, X. Zhao, Y. Lin, H. Y. Xu, and Y. Liu, A stacked memristive device enabling both analog and threshold switching behaviors for artificial leaky integrate and fire neuron, *IEEE Electron Device Lett.* 43(9), 1436 (2022)

12. J. Bian, Z. Liu, Y. Tao, Z. Wang, X. Zhao, Y. Lin, H. Y. Xu, and Y. Liu, Advances in memristor based artificial neuron fabrication-materials, models, and applications, *Int. J. Extreme Manuf.* 6(1), 012002 (2024)
13. X. Shan, Z. Liu, Y. Tao, Y. Dong, Z. Wang, J. Bian, X. Zhao, Y. Lin, H. Xu, and Y. Liu, Light-controlled threshold switching memristive neuron devices for color photoreceptor, *IEEE Electron. Device Lett.* 45(10), 1815 (2024)
14. I. Valov, E. Linn, S. Tappertzhofen, S. Schmelzer, J. van den Hurk, F. Lentz, and R. Waser, Nanobatteries in redox-based resistive switches require extension of memristor theory, *Nat. Commun.* 4(1), 1771 (2013)
15. N. A. Ahir, A. V. Takaloo, K. A. Nirmal, S. S. Kundale, M. Y. Chougale, J. Bae, D. Kim, and T. D. Dongale, Capacitive coupled non-zero I–V and type-II memristive properties of the $NiFe_2O_4$-TiO_2 nanocomposite, *Mater. Sci. Semicond. Process.* 125, 105646 (2021)
16. S. Ranjan, B. Sun, G. Zhou, Y. A. Wu, L. Wei, and Y. N. Zhou, Passive filters for nonvolatile storage based on capacitive-coupled memristive effects in nanolayered organic-inorganic heterojunction devices, *ACS Appl. Nano Mater.* 3(6), 5045 (2020)
17. B. Sun, Y. Chen, G. Zhou, Y. Zhou, T. Guo, S. Zhu, S. Mao, Y. Zhao, J. Shao, and Y. Li, A flexible corn starch -based biomaterial device integrated with capacitive-coupled memristive memory, mechanical stress sensing, synapse, and logic operation functions, *Adv. Electron. Mater.* 9(3), 2201017 (2023)
18. J. Wang, Y. Shao, C. Li, B. Liu, and X. Yan, Artificial optoelectronic synapse based on epitaxial $Ba_{0.6}Sr_{0.4}TiO_3$ thin films memristor for neuromorphic computing and image recognition, *Appl. Phys. Lett.* 121, 262104 (2022)
19. X. Yan, H. He, G. Liu, Z. Zhao, Y. Pei, P. Liu, and H. Yan, A robust memristor based on epitaxial vertically aligned nanostructured $BaTiO_3$-CeO_2 films on silicon, *Adv. Mater.* 34(23), 2110343 (2022)
20. C. Li, H. Yu, T. Shu, Y. Zhang, C. Wen, H. Cao, J. Xie, H. Li, Z. Xu, G. Zhang, Z. Yu, H. Li, L. Liu, Y. Shi, F. Qiu, and D. Dai, PZT optical memristors, *Nat. Commun.* 16(1), 6340 (2025)
21. H. J. Kim, M. Kim, K. Beom, H. Lee, C. J. Kang, and T. S. Yoon, A Pt/ITO/CeO_2/Pt memristor with an analog, linear, symmetric, and long-term stable synaptic weight modulation, *APL Mater.* 7(7), 071113 (2019)
22. X. Yan, H. Yan, G. Liu, J. Zhao, Z. Zhao, H. Wang, H. He, M. Hao, Z. Li, L. Wang, W. Wang, Z. Jian, J. Li, and J. Chen, Silicon-based epitaxial ferroelectric memristor for high temperature operation in self-assembled vertically aligned $BaTiO_3$-CeO_2 films, *Nano Res.* 15(10), 9654 (2022)
23. S. Liu, J. Zeng, Q. Chen, and G. Liu, Recent advances in halide perovskite memristors: From materials to applications, *Front. Phys. (Beijing)* 19(2), 23501 (2024)
24. W. Niu, G. Ding, Z. Jia, X. Ma, J. Zhao, K. Zhou, S. Han, C. Kuo, and Y. Zhou, Recent advances in memristors based on two-dimensional ferroelectric materials, *Front. Phys. (Beijing)* 19(1), 13402 (2024)
25. L. Du, Z. Wang, and G. Zhao, Novel intelligent devices: Two-dimensional materials based memristors, *Front. Phys. (Beijing)* 17(2), 23602 (2022)
26. H. Dou, M. Hellenbrand, M. Xiao, Z. Hu, S. Kunwar, A. Chen, J. L. MacManus-Driscoll, Q. Jia, and H. Wang, Engineering of grain boundaries in CeO_2 enabling tailorable resistive switching properties, *Adv. Electron. Mater.* 9(5), 2201186 (2023)
27. X. Ji, Z. Dong, C. S. Lai, and D. Qi, A brain-inspired in-memory computing system for neuronal communication via memristive circuits, *IEEE Commun. Mag.* 60(1), 100 (2022)
28. X. Ji, Z. Dong, G. Zhou, C. S. Lai, and D. Qi, MLG-NCS: Multimodal local-global neuromorphic computing system for affective video content analysis, *IEEE Trans. Syst. Man Cybern. Syst.* 54(8), 5137 (2024)
29. X. Ji, Y. Chen, J. Wang, G. Zhou, C. S. Lai, and Z. Dong, Time-frequency hybrid neuromorphic computing architecture development for battery state-of-health estimation, *IEEE Internet. Things. J.* 11(24), 39941 (2024)
30. S. Mao, B. Sun, T. Yu, W. Mao, S. Zhu, Y. Ni, H. Wang, Y. Zhao, and Y. Chen, pH-Modulated memristive behavior based on an edible garlic-constructed bio-electronic device, *New J. Chem.* 43(24), 9634 (2019)
31. S. Ranjan, B. Sun, G. Zhou, Y. A. Wu, L. Wei, and Y. N. Zhou, Passive filters for nonvolatile storage based on capacitive-coupled memristive effects in nanolayered organic–inorganic heterojunction devices, *ACS Appl. Nano Mater.* 3(6), 5045 (2020)
32. G. Zhou, J. Wu, L. Wang, B. Sun, Z. Ren, C. Xu, Y. Yao, L. Liao, G. Wang, S. Zheng, P. Mazumder, S. Duan, and Q. Song, Evolution map of the memristor: From pure capacitive state to resistive switching state, *Nanoscale* 11(37), 17222 (2019)
33. S. Zhu, B. Sun, Y. Chen, T. Li, G. Zhou, H. Zhao, and Y. Zhao, An excellent pH-controlled resistive switching memory device based on self-colored ($C_7H_7O_4N$) n extracted from a lichen plant, *J. Mater. Chem. C Mater. Opt. Electron. Devices* 7(25), 7593 (2019)
34. S. G. Hu, Y. Liu, T. P. Chen, Z. Liu, Q. Yu, L. J. Deng, Y. Yin, and S. Hosaka, Emulating the paired-pulse facilitation of a biological synapse with a NiO_x-based memristor, *Appl. Phys. Lett.* 102, 183510 (2013)
35. I. Valov, E. Linn, S. Tappertzhofen, S. Schmelzer, J. van den Hurk, F. Lentz, and R. Waser, Nanobatteries in redox-based resistive switches require extension of memristor theory, *Nat. Commun.* 4(1), 1771 (2013)
36. M. S. Kadhim, F. Yang, B. Sun, W. Hou, H. Peng, Y. Hou, and Y. Zhao, Existence of resistive switching memory and negative differential resistance state in self-colored MoS_2/ZnO heterojunction devices, *ACS Appl. Electron. Mater.* 1(3), 318 (2019)
37. X. Yan, Y. Pei, H. Chen, J. Zhao, Z. Zhou, H. Wang, and P. Zhou, Self-assembled networked PbS distribution quantum dots for resistive switching and artificial synapse performance boost of memristors, *Adv. Mater.* 31(7), 1805284 (2019)
38. C. Zhang, W. B. Ye, K. Zhou, H. Y. Chen, J. Q. Yang, G. Ding, X. Chen, Y. Zhou, L. Zhou, F. Li, and S. T. Han, Bioinspired artificial sensory nerve based on nafion memristor, *Adv. Funct. Mater.* 29(20), 1808783 (2019)
39. S. Seo, J. J. Lee, H. J. Lee, H. W. Lee, S. Oh, J. J. Lee,

K. Heo, and J. H. Park, Recent progress in artificial synapses based on two-dimensional van der Waals materials for brain-inspired computing, *ACS Appl. Electron. Mater.* 2(2), 371 (2020)

40. L. Shao, H. Wang, Y. Yang, Y. He, Y. Tang, H. Fang, J. Zhao, H. Xiao, K. Liang, M. Wei, W. Xu, M. Luo, Q. Wan, W. Hu, T. Gao, and Z. Cui, Optoelectronic properties of printed photogating carbon nanotube thin film transistors and their application for light-stimulated neuromorphic devices, *ACS Appl. Mater. Interfaces* 11(12), 12161 (2019)
41. Y. Wang, Z. Zhang, M. Xu, Y. Yang, M. Ma, H. Li, J. Pei, and L. Shi, Self-doping memristors with equivalently synaptic ion dynamics for neuromorphic computing, *ACS Appl. Mater. Interfaces* 11(27), 24230 (2019)
42. B. Sun, M. Xiao, G. Zhou, Z. Ren, Y. N. Zhou, and Y. A. Wu, Non–zero-crossing current-voltage hysteresis behavior in memristive system, *Mater. Today Adv.* 6, 100056 (2020)